Magnetic Resonance Imaging 32 (2014) 1377–1389

Contents lists available at ScienceDirect

Magnetic Resonance Imaging

journal homepage: www.mrijournal.com

# Exploiting the wavelet structure in compressed sensing MRI

Chen Chen, Junzhou Huang *

*Department of Computer Science and Engineering, University of Texas at Arlington, 500 UTA Boulevard, Arlington, TX, 76019*

ARTICLE INFO

*Article history:*
Received 28 December 2013
Revised 16 March 2014
Accepted 24 July 2014

*Keywords:*
Sparse MRI
Compressed sensing MRI
Tree sparsity
Wavelet tree structure
Structured sparsity

ABSTRACT

Sparsity has been widely utilized in magnetic resonance imaging (MRI) to reduce k-space sampling. According to structured sparsity theories, fewer measurements are required for tree sparse data than the data only with standard sparsity. Intuitively, more accurate image reconstruction can be achieved with the same number of measurements by exploiting the wavelet tree structure in MRI. A novel algorithm is proposed in this article to reconstruct MR images from undersampled k-space data. In contrast to conventional compressed sensing MRI (CS-MRI) that only relies on the sparsity of MR images in wavelet or gradient domain, we exploit the wavelet tree structure to improve CS-MRI. This tree-based CS-MRI problem is decomposed into three simpler subproblems then each of the subproblems can be efficiently solved by an iterative scheme. Simulations and in vivo experiments demonstrate the significant improvement of the proposed method compared to conventional CS-MRI algorithms, and the feasibleness on MR data compared to existing tree-based imaging algorithms.



## 1. Introduction

Magnetic resonance imaging provides a non-invasive manner to aid clinic diagnosis while its limitation is the slow scanning speed. Local motions e.g. breathing, heart beating during the long time scanning may result in ghosting, smearing, streaking on the reconstructed MR image. Parallel MRI (pMRI) [1–5] and compressed sensing MRI [6] techniques are developed to reduce MR scanning time by undersampling. CS-MRI addresses the issue of recovering images from undersampled k-space data based on compressed sensing (CS) theory [7,8], while the image domain pMRI methods (e.g. SENSE [1]) reconstruct the field of view (FOV) by the aliased images obtained from all coils. This difference makes it possible to combine them in the two-step CS-SENSE scheme to further accelerate MRI scanning [9]. After data are acquired by hardware, the k-space data are first recovered by CS-MRI methods to aliased images, and then final FOV is unfolded by SENSE from all the aliased images in the first step.

Although both steps are essential to rapid MRI, CS-MRI attracts more attentions recently due to the emerging of CS and sparsity theories and a lot of efficient algorithms (e.g. FISTA [10] and SPGL1 [11]). SparseMRI [6] is the first work to reconstruct MR images from undersampled data based on CS theory, which models MR image reconstruction as a linear combination of least square fitting, wavelet sparsity and total variation (TV) regularization. The non-smooth terms in their model are smoothed with positive smoothing parameters, and then the whole problem is solved by conjugate gradient (CG) method. To improve the reconstruction accuracy and speed, TVCMRI [12] and RecPF [13] use an operator-splitting method and a variable splitting method to solve this problem respectively. FCSA [14,15] decomposes the original problem into two easy subproblems and separately solves each of them with FISTA [10,16]. They are the state-of-the-art algorithms for CS-MRI. However, such methods may be still limited in clinic MRI due to their reconstruction speed and accuracy. Therefore, algorithms that are both efficient and accurate are quite desirable.

It can be observed that all of the above methods solve the same model as SparseMRI, where the structure of wavelet coefficients is not exploited. Actually, the wavelet coefficients of MR images are not only compressible, but also yield a hierarchical quadtree structure, which is widely applied on image compression [17,18] and signal processing [19]. A typical relationship in the wavelet tree structure is that, if a parent coefficient has a large/small value, its children also tend to be large/small. Recent works on structured sparsity show that the sampling bound could be reduced to $\mathcal{O}(K + log(N/K))$ by fully exploiting the tree structure instead of $\mathcal{O}(K + Klog(N/K))$ for standard sparsity [20,21], where $K$ represents the non-zero elements of the sparse data and $N$ is the length of the data. This benefit can also be interpreted as that tree sparsity-inducing penalties encourage tree structure compared with standard sparsity penalties [22,23]. Intuitively, less k-space data are required for the same reconstruction quality, or more accurate reconstruction can be achieved for the same number of k-space samples. Some methods have been proposed to improve compressed sensing imaging by utilizing the tree sparse prior and generally can be divided into three types:

* Corresponding author.
*E-mail address:* jzhuang@uta.edu (J. Huang).

http://dx.doi.org/10.1016/j.mri.2014.07.016
0730-725X/

greedy algorithms [20,21,24], convex programming [25] and Bayesian learning [26–28]. Although these algorithms provide better reconstruction accuracy than those with standard sparsity, they are slow in general due to the intricate tree structure. Apart from this, the sampling matrix is partial Fourier transform in CS-MRI but not random Gaussian matrix that they assumed. Finally, these methods have been validated only on real-valued images while practical MR data are complex-valued. Therefore, no evidence can guarantee the success of these methods in MRI.

In this article, we propose a new model to improve conventional CS-MRI [6,12–15], where the tree sparsity is combined with standard sparsity and total variation seamlessly. We approximate the tree sparsity as overlapping group sparsity [29]. Due to trade-off between accuracy and computational cost, every coefficient and its parent coefficient are assigned into one group, which force them to be zeros or non-zeros simultaneously. With this configuration, the algorithm will encourage the reconstructed wavelet coefficients to be tree-sparse, but not randomly distributed as by standard sparsity. To solve this overlapping group sparsity problem, an auxiliary variable is introduced to decompose it to three simpler subproblems. Then each of subproblems has a closed form solution or can be solved efficiently by existing techniques. After the data from each coil are reconstructed in the image domain, it is easy to combine pMRI method (e.g. SENSE) in practical applications. Numerical simulations and in vivo experiments on human brain MR data demonstrate that the proposed method always outperforms previous methods on various MR images in terms of both accuracy and computational cost. Some preliminary results have been presented in NIPS2012 [30].

The remainder of the paper is organized as follows. In the next section, we will review the conventional model in CS-MRI and existing tree-based imaging algorithms. In Section 3, our algorithm for CS-MRI is present. Experimental results are presented in Section 4, with comparisons to the state-of-the-art CS-MRI algorithms and tree-based imaging algorithms. Finally, we provide our conclusions in Section 5.

## 2. Related work

### 2.1. CS-MRI

Generally, MR images are sparse in the wavelet domain and the gradient domain, and can be reconstructed with sub-Nyquist-Shannon sampling ratio based on compressed sensing theory. The MRI is first modeled as a CS problem in SparseMRI [6]. Suppose $b$ is the undersampled k-space data, $A$ is the sampling matrix (partial Fourier transform in MRI), then the CS-MRI can be formulated as the linear combination of a least square fitting, total variation and wavelet sparsity regularization:

$$\hat{x} = \arg\min_x \left\{ \frac{1}{2}\|Ax-b\|_2^2 + \alpha\|x\|_{TV} + \beta\|\Phi x\|_1 \right\} \quad (1)$$

where $\alpha$ and $\beta$ are two positive parameters, $x$ is the image to be reconstructed and $\Phi$ denotes the wavelet transform. $\|x\|_{TV} = \sum_i \sum_j \sqrt{(\nabla_1 x_{ij})^2 + (\nabla_2 x_{ij})^2}$, where $\nabla_1$ and $\nabla_2$ denote the forward finite difference operators on the first and second coordinates. Due to the non-smoothness of $\ell_1$ norm and total variation, there is no closed form solution for this problem.

In SparseMRI, the non-smooth terms are transformed to smooth ones by introducing positive smoothing parameters. For example, $\|\Phi x\|_1 \approx \sqrt{(\Phi x)^T(\Phi x) + \mu}$ where $\mu$ is positive and close to zero. Then the approximated problem is solved by classical conjugate gradient (CG) method. Recently, two fast methods TVCMRI [12] and RecPF [13] use an operator-splitting method and a variable splitting method to solve this problem respectively. Both of them have lower time complexity in each iteration, which can substantially reduce the reconstruction time. Accelerated by FISTA [10,16], FCSA [14,15] decomposes the original problem into two subproblems, and then each of them can be solved by existing techniques or has closed form solution. Apart from these, some methods tried to reconstruct compressed MR images by performing $\ell_p$-quasinorm ($p < 1$) regularization optimization [31–33], which are relatively slow although a little bit of higher compression ratio can be achieved. Overall, all the above methods only improve CS-MRI on the algorithmic level. No structured prior information is utilized other than sparsity.

### 2.2. Tree based imaging algorithms

With the emerging of structured sparsity theories [20,21], the required sampling bound has been proven to be lower when some structured prior information is utilized. Typically, it could be reduced to $\mathcal{O}(K + log(N/K))$ if the data follow the hierarchical tree structure. Motivated by the wavelet quadtree structure (Fig. 1), many algorithms have been proposed to improve CS imaging.

For greedy algorithms, model-based CoSaMP [20] utilizes the condensing sort and select algorithm (CSSA) [34] to approximate the wavelet tree structure. Based on OMP [35], StructOMP [21] and

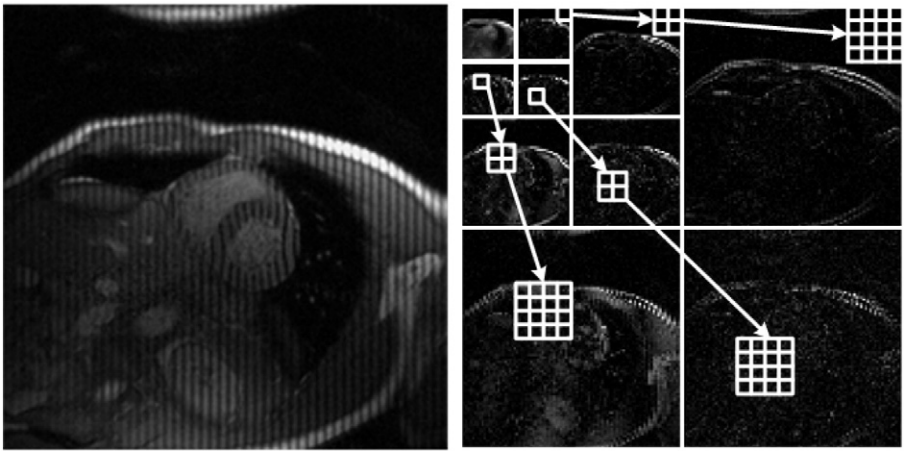

**Fig. 1.** Wavelet quadtree structure. Left: A tagged cardiac MR image. Right: The corresponding wavelet coefficients and quadtree structure.

TOMP [24] are developed for exploiting tree structure where the coefficients are updated by only searching the subtree blocks instead of all subspaces. For Bayesian compressive sensing, the parameter of the distribution of a child node is determined by the distribution of its parent. Markov Chain Monte Carlo (MCMC) [26] and Variational Bayesian (VB) [27] are applied to solve the hierarchical Bayesian models. For approximate message passing (AMP) algorithm [28], the wavelet coefficients are modeled as conditionally Gaussian with variances that depend on the values of hidden Markov tree (HMT) states. Therefore the beliefs (about both coefficients and states) on the corresponding factor graph are propagated. Although all of these methods show significant enhancements in CS imaging than the corresponding methods without tree sparsity, they have general shortcomings (e.g. slow, no global convergence rate) that would slow down MRI reconstruction or may be not feasible at all in practice.

A convex approach is proposed to approximate the hierarchical tree structure with overlapping groups [25]. Every wavelet coefficient and its parent coefficient on the tree are assigned into one group. The formulation of their model can be written as:

$$\hat{\theta} = arg\min_{\theta}\left\{ F(\theta) = \frac{1}{2}\left\|b - A\Phi^T\theta\right\|_2^2 + \lambda_g \sum_{g\in\mathcal{G}} \left\|\tilde{\theta}_g\right\|_2 + \frac{1}{2}\tau^2 \sum_{i=1}^{n}\sum_{j\in J_i}\left(\theta_i - \theta_i^j\right)^2 \right\} \tag{2}$$

where $\mathcal{G}$ denotes the set of all parent–child groups for the wavelet quadtree and $g$ is one of such groups. $\theta$ is a set of the wavelet coefficients, and $\Phi^T$ denotes the inverse wavelet transform. $\tilde{\theta}$ is an extended vector of $\theta$ by replicating the overlapped coefficients. $J_i$ denotes the set of replicated coefficients for $\theta_i$, and the last term is a penalty to force the replicates to be consistent. When wavelet coefficients are recovered, they can be transformed to the recovered image by an inverse wavelet transform. Although tree structure is utilized in their model, it is still hard to be comparable with the state-of-the-art standard sparsity algorithms when applied in CS-MRI. First, the parent–child relationship in their formulation is hard to maintain. Also, it applies SpaRSA [36] to solve (2) which has a relative slow convergence rate of $\mathcal{O}(1/n)$ in terms of function value compared to FISTA with $\mathcal{O}\left(1/n^2\right)$ [16].

Since the tree sparsity can be approximated as overlapping group sparsity, the fastest convex solvers for overlapping group sparsity should also be introduced and compared. SLEP [37] (sparse learning with efficient projections) has the package for overlapping group lasso. Its main function is to iteratively solve the tree structured denoising problem by selecting active groups. When it comes to reconstruction problem, it applies proximal methods (e.g. FISTA) to transfer the problem to denoising. Another solver YALL1 [38] first relaxes the constrained overlapping group minimization to unconstrained problem by Lagrangian method. Then the minimization of the $x$ and $z$ subproblems can be written as:

$$\hat{x} = arg\min_{x,z}\left\{ \frac{\beta_2}{2}\|Ax-b\|_2^2 + \lambda_1^T G\Phi x + \frac{\beta_1}{2}\|z - G\Phi x\|_2^2 - \lambda_2^T Ax + \sum_{i=1}^{s} w_i\|z_i\|_2 \right\} \tag{3}$$

where $G$ is a binary matrix to indicate the group configuration; $s$ is the total number of groups. $\lambda_1$, $\lambda_2$ are multipliers and $\beta_1$, $\beta_2$ are positive parameters. $w_i$ denotes the weight for each $z_i$, which can be set as 1 for simpleness. All the above tree-based algorithms assume strong tree sparsity, which may not be strictly satisfied on practical MR data.

## 3. Tree based CS-MRI

### 3.1. Algorithm

The classical CS-MRI model [6] combines wavelet sparsity and total variation regularization. Most existing tree-based compressed sensing algorithms directly replace the standard sparsity with tree sparsity [25–28,37,38]. However, for practical MR images, the wavelet coefficients cannot perfectly match the theoretical assumption of tree sparsity. Therefore, we introduce one more regularization term in previous model with tree sparsity. It is assumed that MR images tend to follow all of the sparse prior information. We approximate the tree structure with overlapping groups as previous work [25]. Tree-based CS-MRI problem can be formulated as follows:

$$\min_x\left\{ F(x) = \frac{1}{2}\|Ax-b\|_2^2 + \alpha\|x\|_{TV} + \beta\left( \|\Phi x\|_1 + \sum_{g\in\mathcal{G}}\left\|(\Phi x)_g\right\|_2 \right) \right\} \tag{4}$$

The total variation and wavelet sparse term in fact have complemented the tree structure assumption on real data, which make our model more robust on practical MR images. This is a main difference with previous tree structured models. When the image cannot follow the tree sparsity assumption strictly, the performance of all previous methods may suffer. We call the proposed method as Wavelet Tree Sparsity MRI (WaTMRI). Fig. 2 shows the performance of the proposed method on the tagged cardiac image after removing

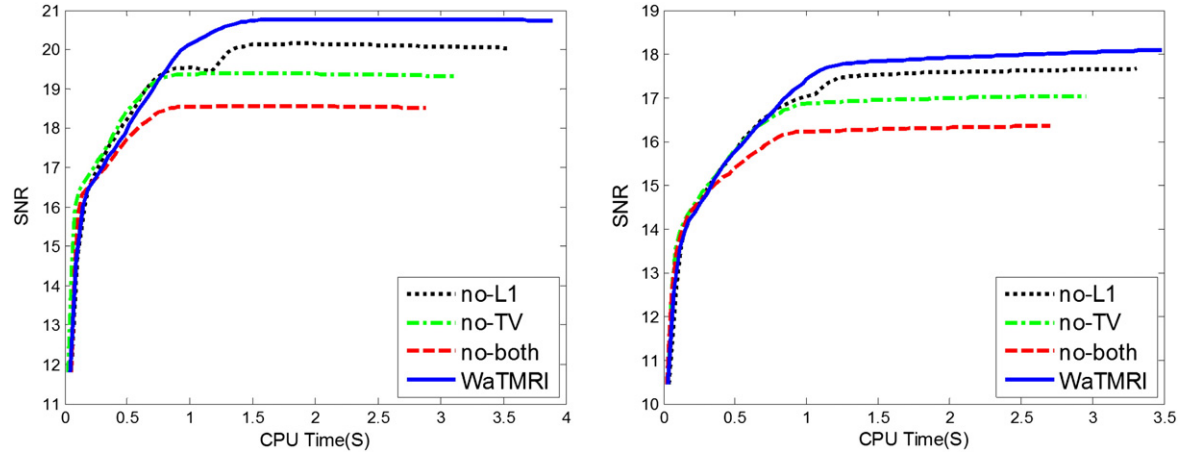


**Fig. 2.** Performance of the proposed method without combining $\ell_1$ norm, without combining TV or without combining both. The left one is with 25% sampling for the cardiac image in Fig. 1, and the right one is with 20% sampling for the same image.

TV, $\ell_1$ norm of wavelet sparsity, or both. Same trend has been observed on all the other images that tested in the experiments.

We introduce an auxiliary variable $z$ to constrain the wavelet coefficients $\Phi x$ with overlapping. Then the problem becomes non-overlapping convex optimization. Let $G\Phi x = z$, (4) can be rewritten as:

$$\min_{x,z}\left\{F(x)=\frac{1}{2}\|Ax-b\|_2^2+\alpha\|x\|_{TV}+\beta\left(\|\Phi x\|_1+\sum_{i=1}^{s}\left\|z_{g_i}\right\|_2\right)+\frac{\lambda}{2}\|z-G\Phi x\|_2^2\right\} \tag{5}$$

where $G$ is a binary matrix for group configuration. Similar work can be found in YALL1 [38]. There are two variables in (5), which could be easily split. For the $z$ subproblem, it can be written as:

$$z_{g_i}=\arg\min_{z_{g_i}}\left\{\beta\left\|z_{g_i}\right\|_2+\frac{\lambda}{2}\left\|z_{g_i}-(G\Phi x)_{g_i}\right\|_2^2\right\} \tag{6}$$

where $i = 1, 2, \ldots, s$, $g_i$ is the i-th group and $s$ is number of total groups. There is a closed form solution by the group-wise soft thresholding:

$$z_{g_i}=max\left(\|r_i\|_2-\frac{\beta}{\lambda},0\right)\frac{r_i}{\|r_i\|_2}, i=1,2,\ldots,s \tag{7}$$

where $r_i=(G\Phi x)_{g_i}$.

For the $x$ subproblem,

$$x=\arg\min_{x}\left\{\frac{1}{2}\|Ax-b\|_2^2+\alpha\|x\|_{TV}+\beta\|\Phi x\|_1+\frac{\lambda}{2}\|z-G\Phi x\|_2^2\right\} \tag{8}$$

we can combine the first and last quadratic penalty on the right side. Then the rest has the similar form with FCSA and can be solved efficiently with an iterative scheme. Let $f(x)=\frac{1}{2}\|Ax-b\|_2^2+\frac{\lambda}{2}\|z-G\Phi x\|_2^2$, which is a convex and smooth function with Lipschitz $L_f$, and $g_1(x)=\alpha\|x\|_{TV}$, $g_2(x)=\beta\|\Phi x\|_1$, which are convex but non-smooth functions. Then this $x$ problem has the similar form as FCSA [15]:

$$\min_x\{F(x)=f(x)+g_1(x)+g_2(x)\} \tag{9}$$

For convenience, we denote (7) by $z = shrinkgroup\left(G\Phi x,\frac{\beta}{\lambda}\right)$. Now, we can summarize our algorithm as in Algorithm 1:

The proximal map in step 3, 4 is defined for any scaler $\rho > 0$:

$$prox_\rho(g)(x):=\arg\min_u\left\{g(u)+\frac{1}{2\rho}\|u-x\|^2\right\} \tag{10}$$

and $\nabla f(r^n)=A^T(Ar^n-b)+\lambda\Phi^TG^T(G\Phi r^n-z)$ with $A^T$ denotes the inverse partial Fourier transform. More details can be found in FCSA [15].

### 3.2. Algorithm analysis

Suppose $x$ represents an image with $N$ pixels and $z$ is an extended vector with replicated wavelet coefficients, which contains $N'$ elements. Although $G$ is

**Algorithm 1**. WaTMRI

Input: $\rho = 1/L_f$, $r^1 = x^0$, $t^1 = 1$, $\alpha$, $\beta$, $\lambda$

for $n = 1$ to *MaxIteration* do

1) $z = shrinkgroup(G\Phi x^{n-1}, \beta/\lambda)$
2) $x_g = r^n - \rho\nabla f(r^n)$
3) $x_1 = prox_\rho(2\alpha\|x\|_{TV})(x_g)$
4) $x_2 = prox_\rho(2\beta(\|\Phi x\|_1)(x_g)$
5) $x^n = (x_1 + x_2)/2$
6) $t^{n+1}=\left[1+\sqrt{1+4(t^n)^2}\right]/2$
7) $r^n+1 = x^n+\frac{t^{n-1}}{t^{n+1}}(x^n-x^{n-1})$

end fora $N' \times N$ matrix, it is sparse with only $N'$ non-zero elements. So we can implement a multiplication by $G$ efficiently with $\mathcal{O}(N')$ time. Step 1 *shrinkgroup* takes $\mathcal{O}(N' + NlogN)$ time. The total cost of step 2 takes $\mathcal{O}(NlogN)$ time. Step 4 takes $\mathcal{O}(NlogN)$ when the fast wavelet transform is applied. Both step 3 and step 5 cost $\mathcal{O}(N)$. Note that $N' \le 2N$ since we assign every parent–child coefficients to one group and leave every wavelet scaling in one group. So the total computation complexity for each iteration is $\mathcal{O}(NlogN)$, the same complexity as that in TVCMRI, RecPF and FCSA. We introduce the wavelet tree structure constrain in our model, without increasing the total computation complexity. As FISTA has reached the optimal convergence rate for first order methods [39,40], our algorithm also has a very fast convergence rate after accelerated by FISTA.

### 3.3. Extension to parallel MRI

We have introduced the new algorithm for CS-MRI. In this subsection, we will briefly introduce how to combine this method in practical MRI based on CS-SENSE framework [9]. In pMRI, multi-channel coils are used to reduce the sampling ratio. Each coil only acquires partial k-space data to reconstruct the aliased images, and the final FOV is unfolded with the coil profile information. If CS technique is used, further less data are acquired in each coil. Fig. 3 demonstrates the whole procedure. In contrast to SENSE which

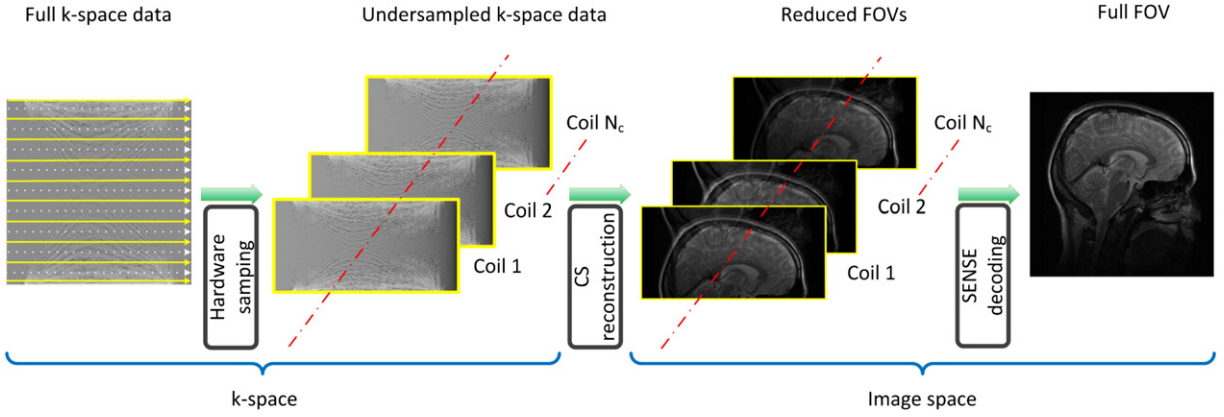


**Fig. 3.** Illustration of basic Cartesian CS-SENSE procedure with Nc coils. The first step is to recover reduced FOVs by CS-MRI algorithms. The second step is to unfold these reduced FOVs to the final image. The solid lines indicate the acquired k-space data and dashed lines denote the nonacquired data.

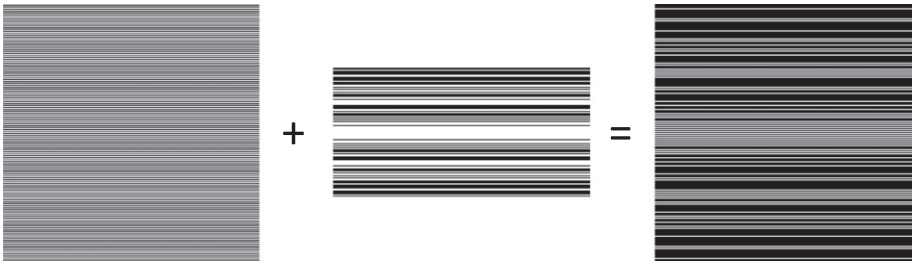

**Fig. 4.** An example of hybrid sampling scheme. The left one is 1/2 sampling in Cartesian SENSE. The middle one is 1/2 sampling in CS. The right one is the final sampling mask with 1/4 sampling.

**Fig. 5.** Sampling masks. From left to right: pseudo-Gaussian mask, random lines mask and pseudo-radial mask.

recovers the reduced FOVs by inverse fast Fourier transform (FFT), CS-SENSE scheme only recovers each aliased image with under-sampled data.

Due to the minimum measurement bound of CS and noises in practice, the sampling ratio cannot be very low if CS or pMRI is only applied alone. However, this hybrid scheme could overcome this shortcoming since MRI is accelerated twice (Fig. 4). We could use CS to reconstruct the aliased image of each coil. Thus, the final FOV can be obtained from these aliased images in the SENSE scheme. The result could be even better after replacing the CS-MRI algorithm in the first step with the proposed tree-based CS-MRI algorithm. Our experimental results shown in the next section validate this advantage of the proposed method.

## 4. Experiments

### 4.1. Experiment setup

We conduct experiments on two data sets: real-valued MR images and MR raw datasets with complex values. All experiments are conducted on a laptop with 2.4GHz Intel core i5 2430 M CPU in MATLAB 2009 (MathWorks, Natick, MA). We first compare our algorithm with the classical CG method [6] and three of the fastest MR image reconstruction algorithms: TVCMRI [12], RecPF [13], FCSA [14,15], and then with general tree based algorithms or solvers: AMP [28], VB [27], YALL1 [38], and SLEP [37]. For fair comparisons, all codes are downloaded from the Websites of the corresponding authors. We do not include MCMC [26] in experiments because it has ultra-slow execution speed and untractable convergence [27,28]. OGL [25] solves its model by SpaRSA [11] with only $\mathcal{O}(1/n)$ convergence rate, which cannot be competitive with recent FISTA [10,16] algorithms with $\mathcal{O}(1/n^2)$ convergence rate. The authors have not published the code yet. So we do not include OGL for comparisons neither. The parameters are tuned for real-valued images and complex-valued image respectively. All measurements are mixed with Gaussian white noise with 0.01 standard deviation (STD). Signal-to-noise ratio (SNR) is used for result evaluation:

$$SNR = 10log_{10}(V_s/V_n) \tag{11}$$

where $V_n$is the mean square error between the original image $x_0$ and the reconstructed $x$; $V_s = var\ (x_0)$ denotes the power level of the original image where $var\ (x_0)$ denotes the variance of the values in $x_0$.

Both Cartesian mask (random lines) and non-Cartesian masks (pseudo-Gaussian random mask and pseudo-radial mask) are used for experiments. For the pseudo-Gaussian mask, we follow the sampling strategy of previous works [12,14,15], which randomly choose more Fourier coefficients from low frequency and less on high frequency. For Cartesian mask and pseudo-radial mask, we follow SparseMRI [6] and RecPF [13] respectively. The examples of these masks are shown in Fig. 5.

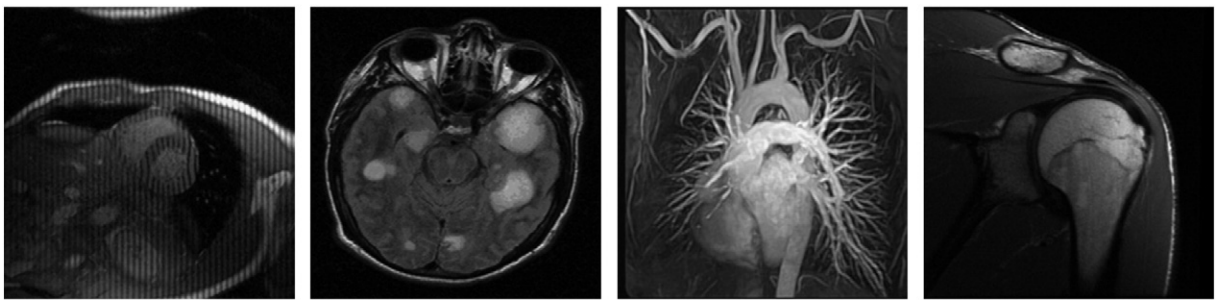

**Fig. 6.** MR images. From left to right: cardiac; brain; chest; shoulder.

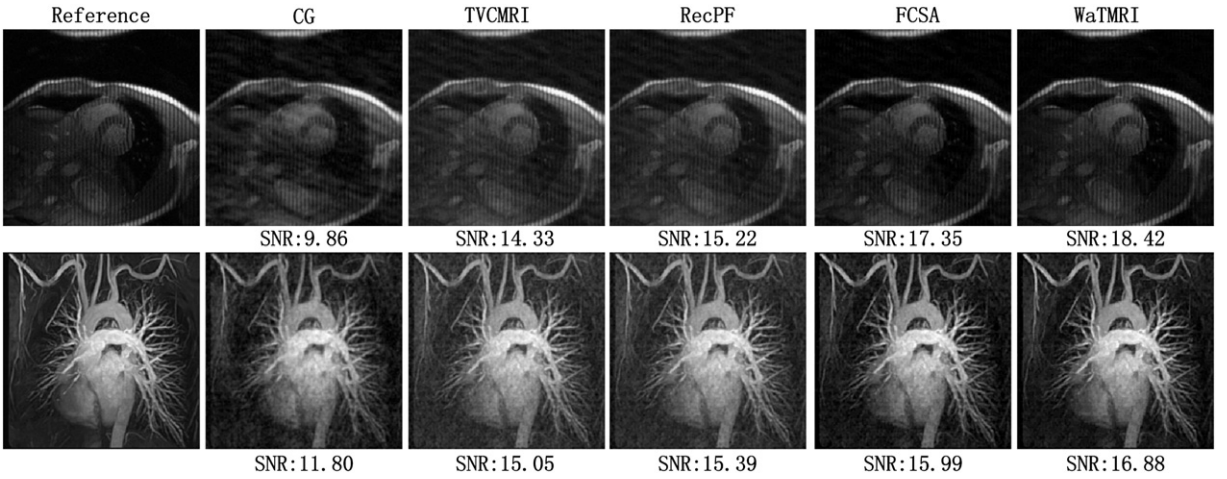


**Fig. 7.** Visual comparisons among the state-of-the-art MR image reconstruction algorithms with 20% sampling. The results on the "cardiac" image are shown in the first row. The results on the "chest" image are shown in the second row.

*4.1.1. Real-valued MR images*

As most existing tree-based imaging algorithms could only support real number input, we conduct experiments on four MR images with real value. They are from different organs of human: cardiac, brain, chest and shoulder (Fig. 6). For convenience, all test images are resized to 256 × 256, and the wavelet decomposition level is 4. Suppose the partial Fourier transform with $M$ rows and $N$ columns, the sampling ratio is defined as M/N.

*4.1.2. Complex-valued human brain image*

To validate the proposed algorithm in practical MRI, we also conduct experiments on multi-channel MR raw datasets. The first image is an axial brain image from a 3 T commercial scanner (GE Healthcare, Waukesha, WI) with an eight-channel head coil (In Vivo, Gainesville, FL) using a two-dimensional T1-weighted spin echo protocol (TE/TR = 11/700 ms, 22-cm FOV, 10 slices, 256 × 256 matrix) [9]. The second one is a T1-weighted image from spoiled

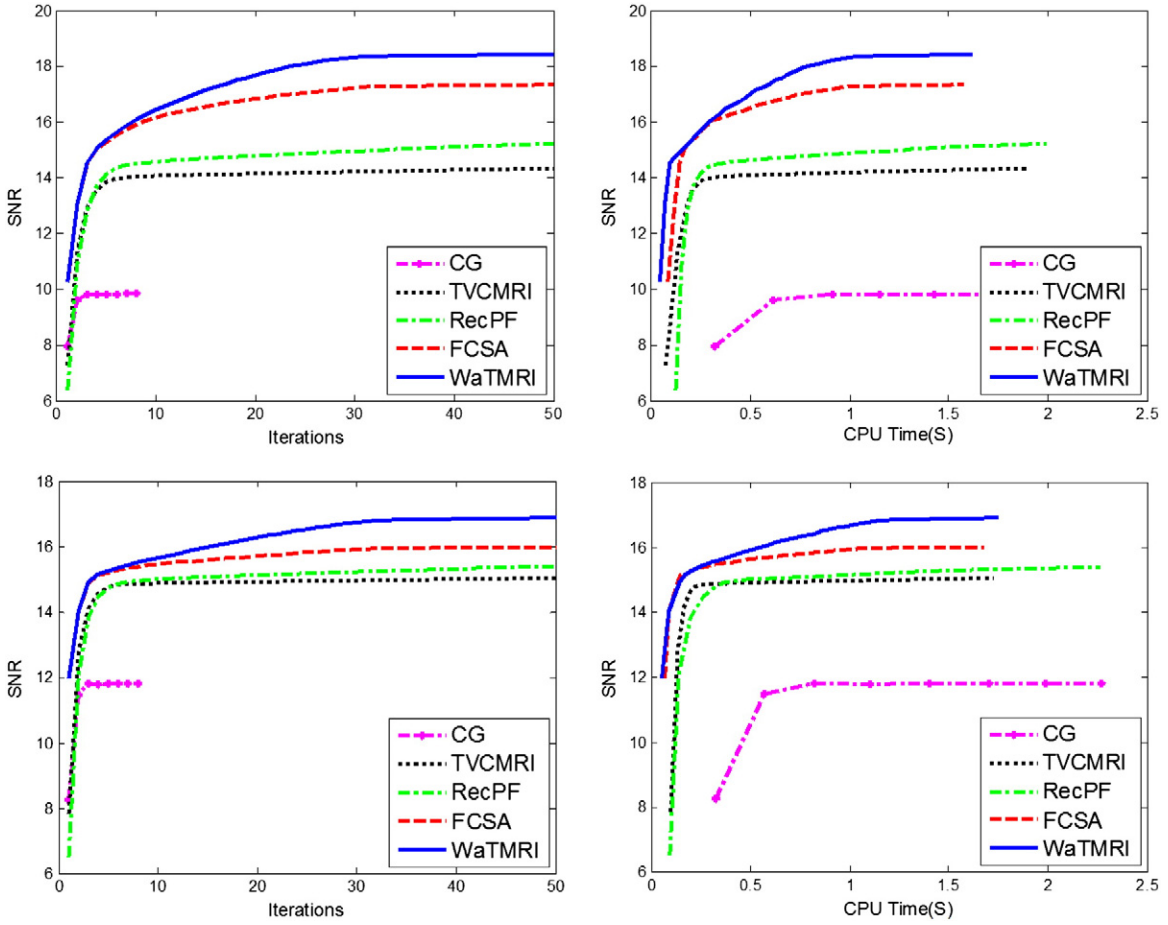


**Fig. 8.** The average convergence speed in terms of SNR. The first row is the comparison on the "cardiac" image. The second row is the comparison on the "chest" image.

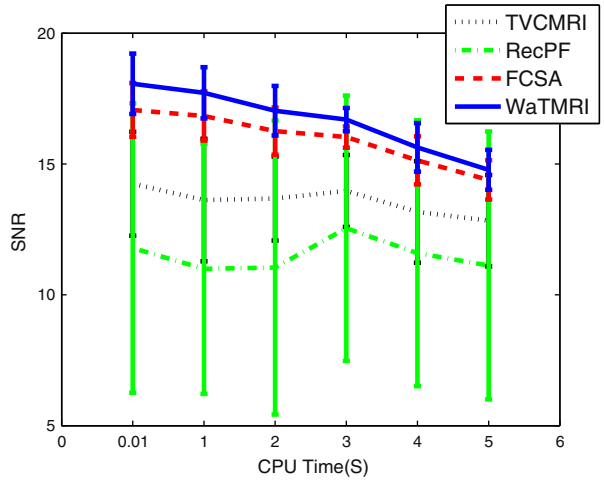


**Fig. 9.** Comparisons under different noise suppression with 20% sampling. Each bar represents the average SNR on the four MR images.

gradient echo (SPGR) sequence, scanned on a GE Signa-Excitep 1.5-T scanner with an eight-channel receive coil (TE = 8 ms, TR = 17.6 ms, FOV = 20 cm, 200 × 200 pixels) [5].

As TVCMRI [12] and RecPF [13] are always inferior to FCSA in existing work [15] and our previous experiments, they are not compared on this dataset. The date from each coil is reconstructed separately, and the final image is obtained by the sum-of-square (SoS) method. The reference image is reconstructed with full k-space data.

### 4.2. Comparisons with CS-MRI algorithms

#### 4.2.1. Visual comparisons and SNRs

We first compare our method with the state-of-the-art MR image reconstruction algorithms. The sampling mask is the pseudo-Gaussian mask in Fig. 5. All algorithms terminate after 50 iterations as in previous work [15]. Fig. 7 shows the reconstruction result. Due to the high time complexity of CG [6], it only runs 8 iterations for all images with real values. CG [6], TVCMRI [12] and RecPF [13] have not converged under this setting due to their relative slow convergence rate, which has resulted in visible artifacts in the reconstructed images. With sufficient iterations and reconstruction time, they will converge to the same result of FCSA [15]. The visual results recovered by the proposed algorithm are the closest to the original with only 20% sampling ratio, which has the highest SNRs and fewest artifacts. When comparing SNRs (Fig. 8), the proposed algorithm converges the fastest both in iterations and computational time. To reduce randomness, all results are recorded by averaging the values after repeating each experiment 100 times. We have conducted experiments on other images and obtain similar results that the proposed algorithm always has the best performance in terms of SNR and visual result. These results are reasonable because we exploit wavelet tree structure in our model, which can reduce requirement for the number of measurements or increase the accuracy of the solution with the same measurements.

#### 4.2.2. Comparisons under different sampling masks, sampling ratios and noise

Besides the experiments above, we conduct more comprehensive experiments on all the four images. CG [6] is not included in all these experiments due to its higher computational cost. The first one is under different noise suppression. The sampling mask is also the pseudo-Gaussian mask and each algorithm terminates after 50 iterations. Fig. 9 demonstrates the results under 20% sampling with different noises whose standard deviations range from 0.01 to 5. We could observe that WaTMRI is always better than FCSA [14,15], and far better than TVCMRI [12] and RecPF [13]. This is consistent with previous experiments in FCSA [14,15].

To show more statistical results, we conducted experiments on the four MR images under different sampling masks in Fig. 5 with various sampling ratios. Fig. 10 demonstrates these results. Each bar represents the average SNR on these MR images. We could find three trends in this figure: 1), the SNRs of all algorithms drop as the sampling ratio becomes lower; 2), the algorithms perform best under the pseudo-Gaussian mask because it is the most incoherent; 3), at any sampling ratio and mask, the proposed algorithm is always superior to the others. It coincides with the structured sparsity theories that the more correct prior information is utilized, the better reconstruction can be achieved.

### 4.3. Comparisons with general tree based imaging algorithms

We also compare our algorithm with existing tree-based algorithms and overlapping group sparsity solvers for general CS imaging. For statistical algorithms AMP [28] and VB [27], we use the default setting in their code. For SLEP [37], we set the same parameters $\alpha$ and $\beta$ as those in previous experiments. For YALL1 [38], we set both $\beta_1$ and $\beta_2$ equal to $\beta$. Due to the higher space requirement and time complexity of VB, we resize all images to 128 × 128. The wavelet decomposition level is set as 3. Fig. 11 demonstrates the average performance in SNR against computational time with 20% sampling. Due to the higher computational complexity of VB, it is not shown in this figure. All algorithms run 50 iterations except AMP only runs 10 iterations. The proposed WaTMRI always converges the fastest and achieves the highest SNR.

Tables 1 and 2 show the means and STDs of the results on four MR images with 20% sampling. Although statistical algorithms are slow in general, they are not sensitive to the parameters, as most parameters are learned from data. Fortunately, good parameters for MR image reconstruction are easy to tune in our model. Fig. 12

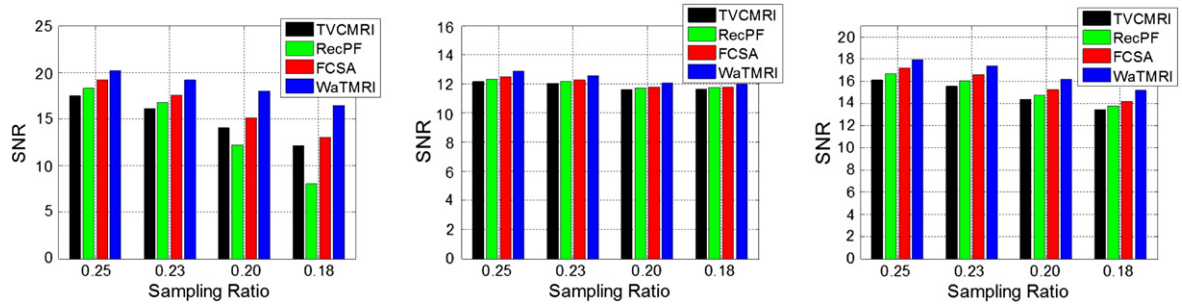


**Fig. 10.** Comparisons with the state of art MR image reconstruction algorithms under different sampling masks with various sampling ratios. From left to right, the results are on pseudo-Gaussian, random lines and pseudo-radial sampling masks.

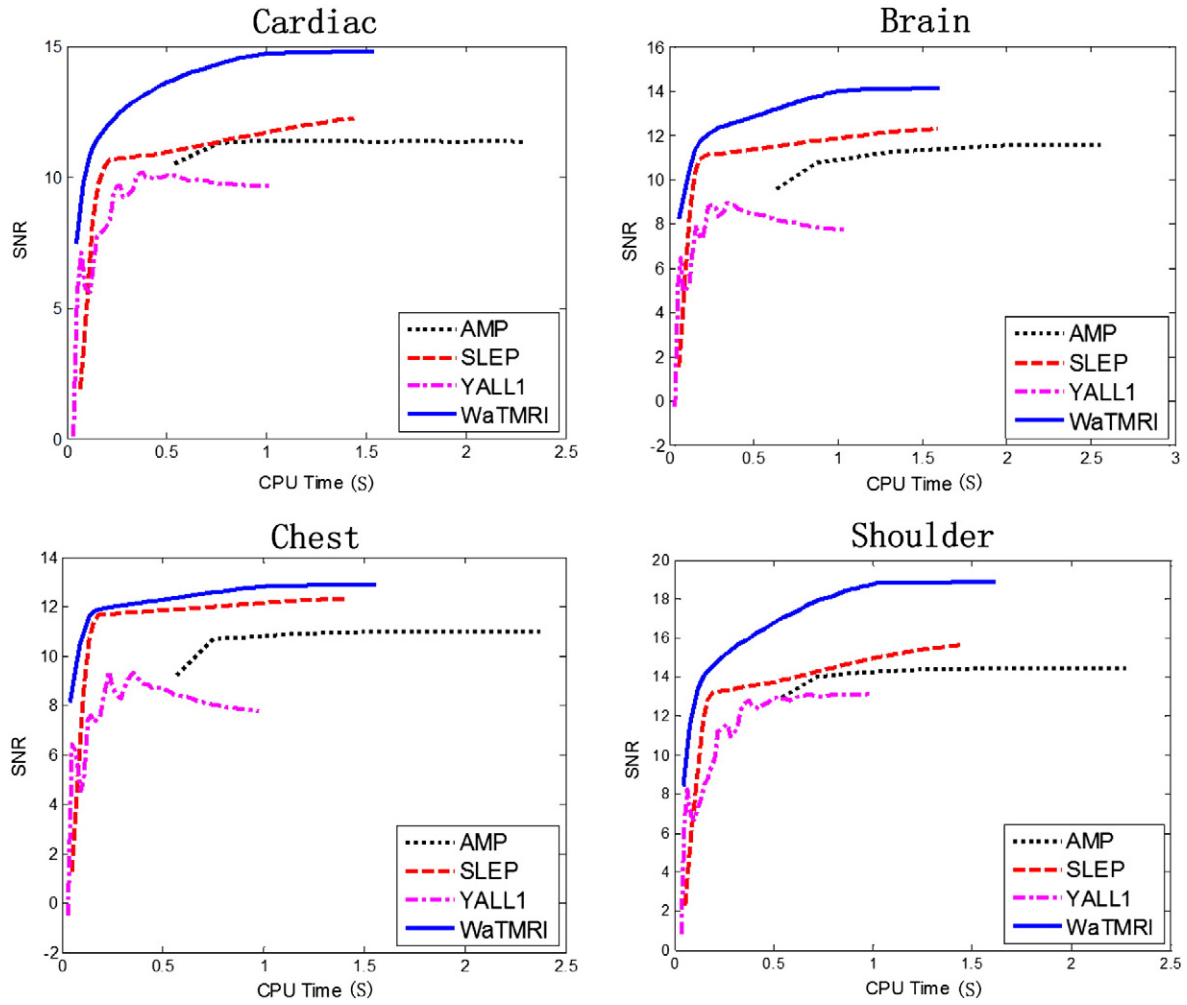


**Fig. 11.** Comparisons with existing tree-based CS algorithms on the four MR images with 20% sampling.

demonstrates the comprehensive performance of the proposed algorithm compared to other tree-based CS algorithms or solver under different sampling ratios and on different images. WaTMRI is always far better than others on CS-MRI.

### 4.4. Comparisons on toy images

Except the proposed algorithm, all other tree-based algorithms have a strong assumption of the tree structure (no total variation and standard sparsity in their models). However for MR images, many images do not strictly follow this assumption, and then their performance may suffer. To validate this, we conduct another experiment on a toy MR image, which is strictly consistent with the tree structure assumption. First we set the wavelet coefficients that have the smallest 0.1% energy to zero. Then if the parent or child of a coefficient is zero, we set this coefficient to be zero. Hence coefficients in the same group are both zeros or non-zeros. The toy image and its wavelet coefficients are presented at Fig. 13. The results of all algorithms on the toy cardiac image are shown in Fig. 14. Compared with CS-MRI algorithms, the proposed algorithm improve a lot, and becomes much better than those without tree sparsity, which validates the effectiveness of the proposed algorithm by utilizing tree sparsity. Compared with tree-based algorithms, the performance difference becomes much smaller, which explains the results of previous experiments. On MR images that do not perfectly satisfy the tree sparsity assumption, the proposed algorithm has great superiority by combining TV and wavelet sparsity real MR images.

### 4.5. Parallel MRI with MR raw data

Besides previous simulations, we also conduct experiments on MR raw datasets. Both datasets contain 8 channel full k-space data with complex values. As discussed above, we only compare the

**Table 1**
Comparisons of SNR (dB) on four MR images.

| Algorithms | Cardiac | Brain | Chest | Shoulder |
|---|---|---|---|---|
| AMP [10] | 11.36 ± 0.95 | 11.56 ± 0.60 | 11.00 ± 0.30 | 14.49 ± 1.04 |
| VB [9] | 9.62 ± 1.82 | 9.23 ± 1.39 | 8.93 ± 0.79 | 13.81 ± 0.44 |
| SLEP [18] | 12.24 ± 1.08 | 12.28 ± 0.78 | 12.34 ± 0.28 | 15.65 ± 1.78 |
| YALL1 [19] | 9.56 ± 0.13 | 7.73 ± 0.15 | 7.76 ± 0.56 | 13.14 ± 0.22 |
| Proposed | **14.80 ± 0.51** | **14.11 ± 0.41** | **12.90 ± 0.13** | **18.93 ± 0.73** |

**Table 2**
Comparisons of execution time(S) on four MR images.

| Algorithms | Cardiac | Brain | Chest | Shoulder |
|---|---|---|---|---|
| AMP [10] | 2.30 ± 0.06 | 2.36 ± 0.33 | 2.37 ± 0.41 | 2.29 ± 0.22 |
| VB [9] | 13.95 ± 0.11 | 14.25 ± 0.29 | 14.11 ± 0.40 | 14.15 ± 0.42 |
| SLEP [18] | 1.44 ± 0.08 | 1.52 ± 0.06 | 1.41 ± 0.05 | 1.45 ± 0.08 |
| YALL1 [19] | 1.02 ± 0.04 | 1.04 ± 0.01 | 0.98 ± 0.04 | 1.00 ± 0.02 |
| Proposed | 1.54 ± 0.04 | 1.61 ± 0.03 | 1.56 ± 0.07 | 1.62 ± 0.14 |

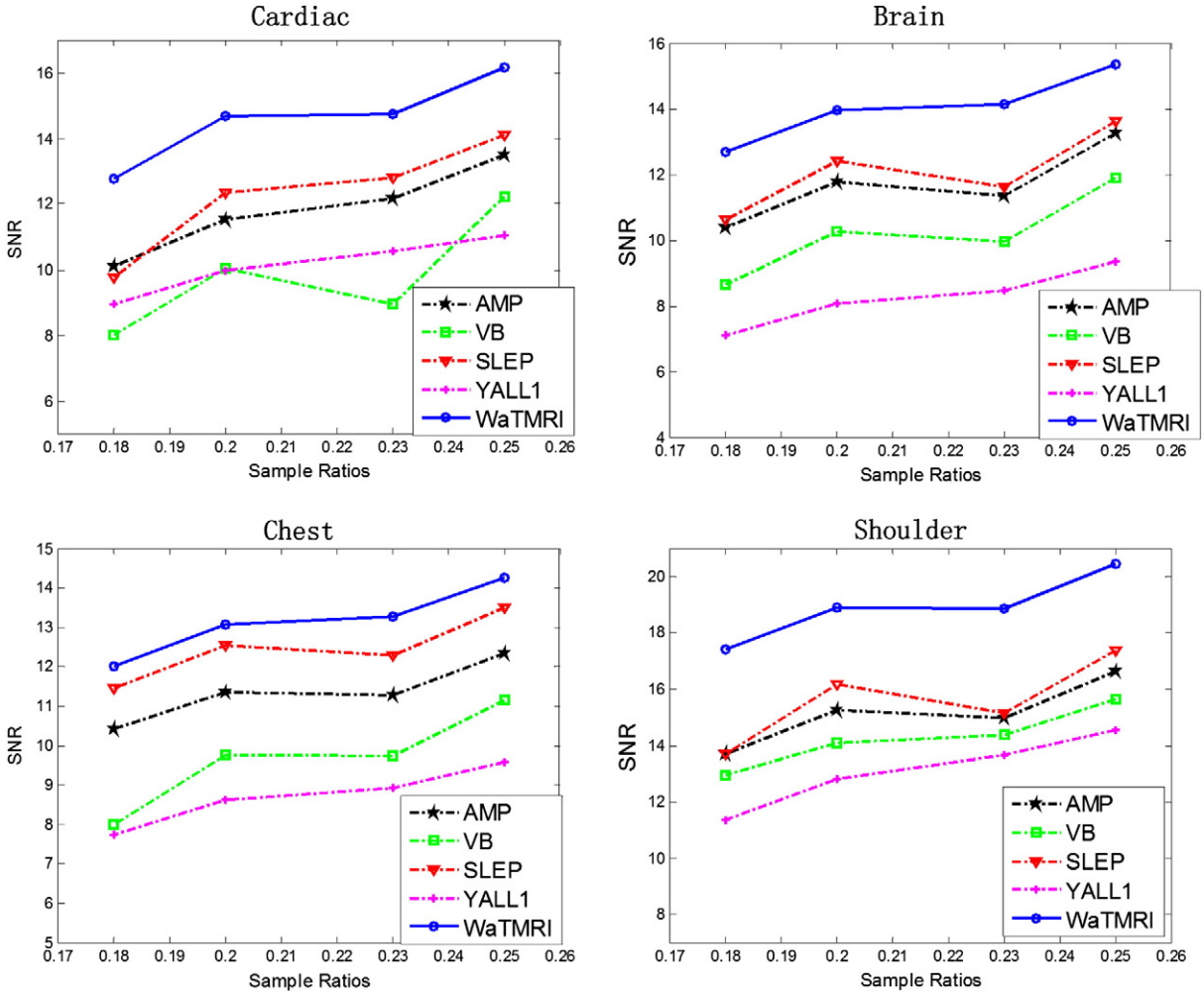


**Fig. 12.** Comparisons with general tree-based imaging algorithms or solvers on the four MR images with different sampling ratios.

proposed algorithm with CG [6] and FCSA [14,15]. Each algorithm runs enough iterations to ensure convergence. Cartesian sampling mask (the middle one of Fig. 5) is used in these experiments, which is the most feasible one in clinic applications. Undersampled data in each coil are used to recover the corresponding aliased image. The final image is obtained by a sum of square scheme with these aliased images. The image obtained by full k-space data is used as reference image for computing SNRs. Figs. 15 and 16 show all the visual results. Both images reconstructed by CG and FCSA have visible artifacts (light spots). For quantitative analysis, the WaTMRI

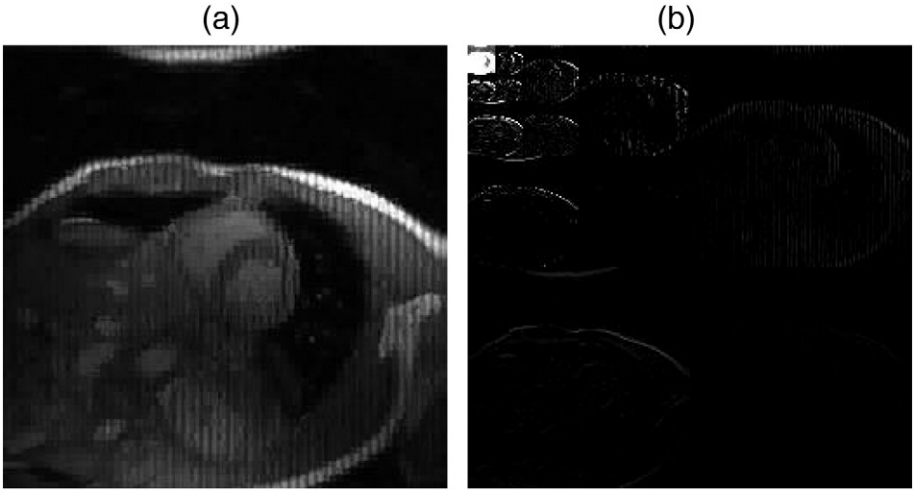


**Fig. 13.** (a) The toy cardiac image; (b) the corresponding wavelet coefficients.

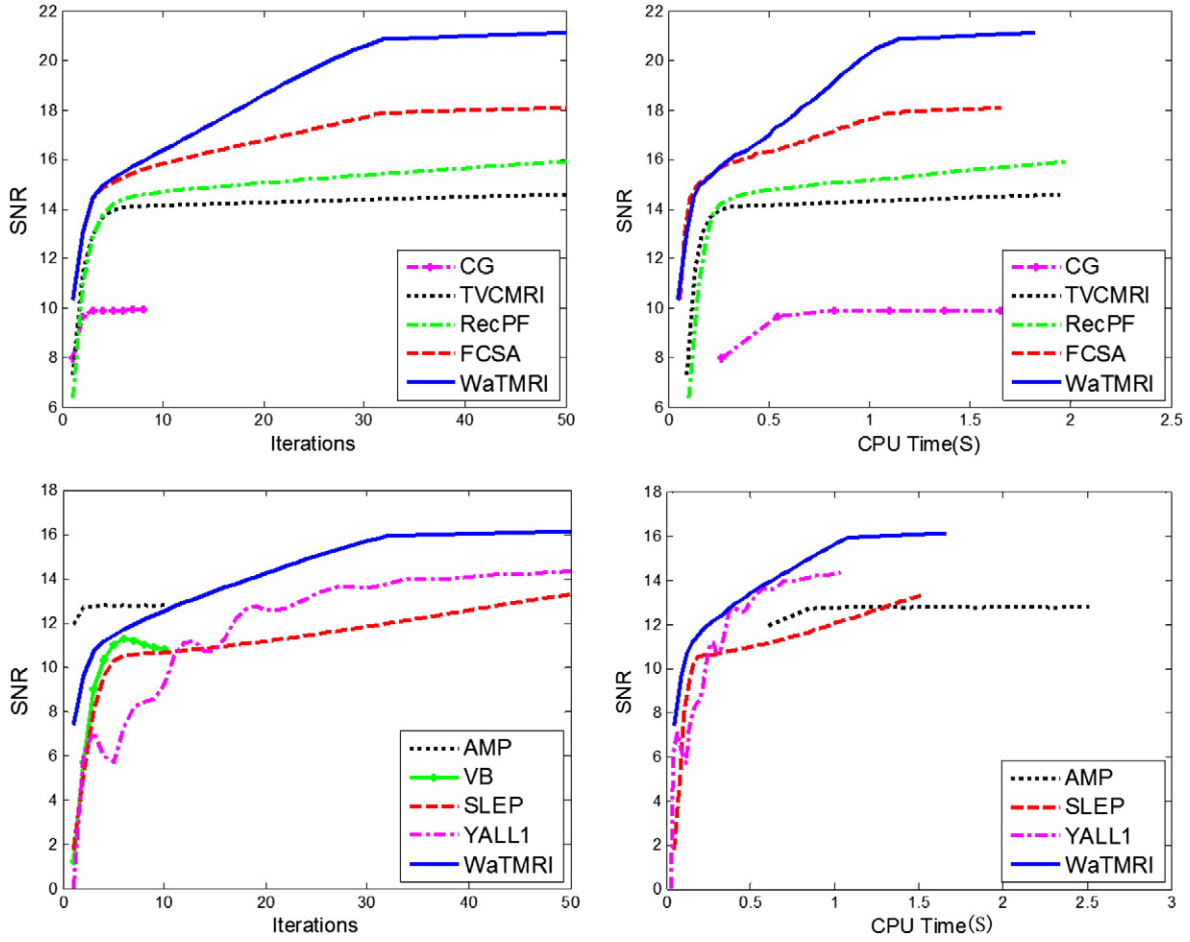


**Fig. 14.** Comparisons with all the algorithms on a "toy cardiac" image with 20% sampling.

achieves the highest SNR and smallest error. The convergence performance is demonstrated in Fig. 17. CG and FCSA converge to similar result as they solve the same problems. The little difference may be caused by different approximation methods. Guaranteed by structured sparsity theories, our methods have significantly better performance. All these demonstrate the superiority of the proposed method in practical MRI.

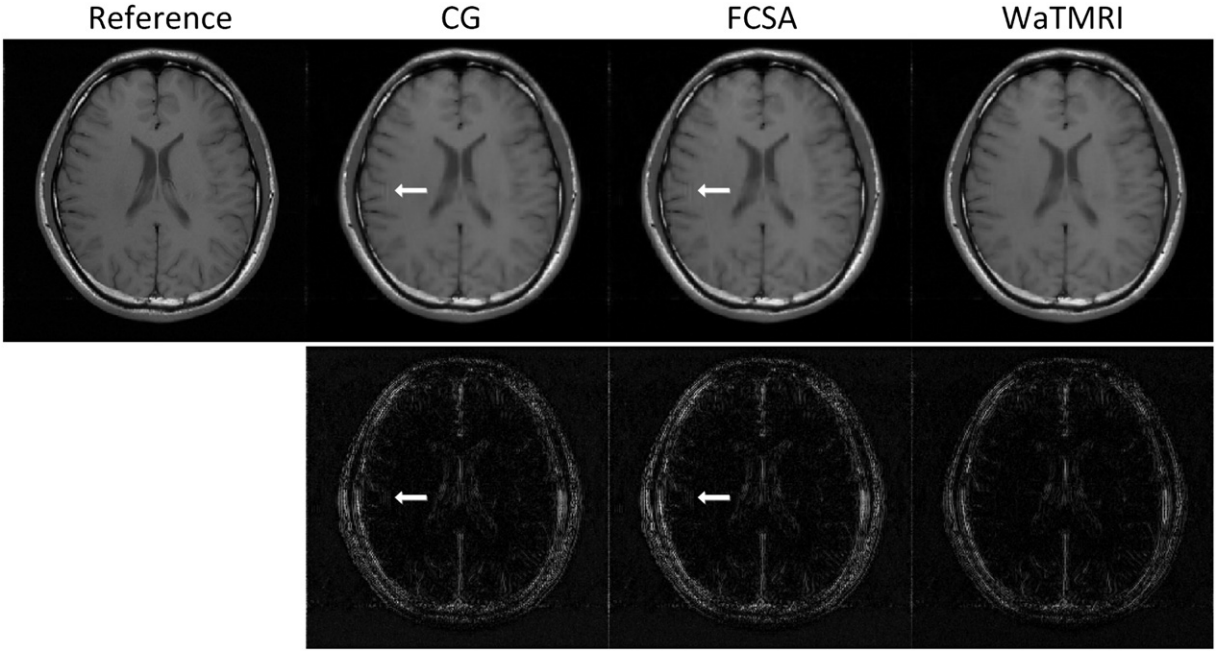


**Fig. 15.** The visual results reconstructed on the 3 T brain image. The first row contains the results reconstructed with 33% sampling. Their SNRs are 19.30, 18.98 and 21.09 respectively. Their relative errors are 0.073 0.076 and 0.059 respectively. White arrows indicate visible artifacts. The second row contains the corresponding error images.

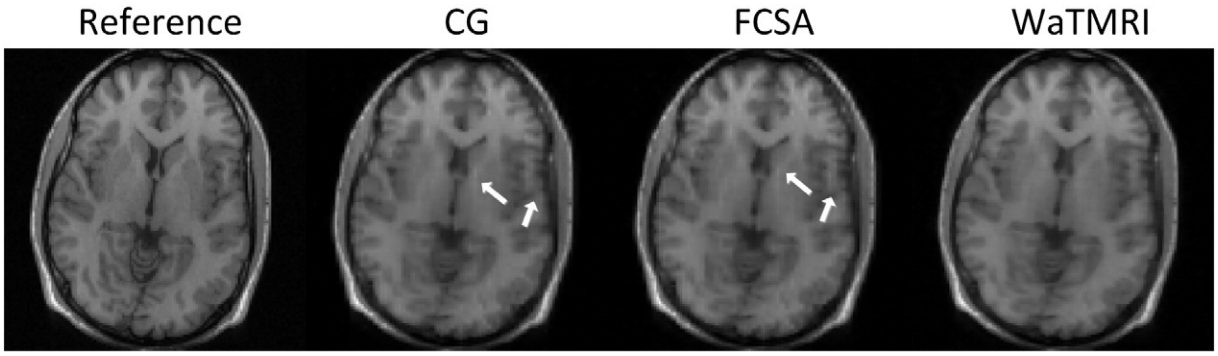


**Fig. 16.** The visual results reconstructed on the 1.5 T brain image with 33% sampling. Their SNRs are 16.65, 16.55 and 17.51 respectively. Their relative errors are 0.091 0.092 and 0.082 respectively. White arrows indicate visible artifacts.

### *4.6. Discussion*

We propose an efficient algorithm WaTMRI to reconstruct the compressed MR images. Besides the regularization terms in conventional model, we utilize tree sparsity to improve CS-MRI. The computational complexity of the WaTMRI is $\mathcal{O}(NlogN)$ in each iteration ($N$ is the pixel number in reconstructed image), which is the same as that in previous algorithms. It has fast convergence property and has been shown to significantly outperform the previous algorithms for CS-MRI and general tree-based imaging algorithms. The experimental results reported above validate the effectiveness and efficiency of the proposed algorithm for CS-MRI.

Some CS-MRI algorithms (e.g. [41,42]) are proposed recently by utilizing double-density dual-tree wavelet transform [43]. Actually, these methods still reconstructed MR images with standard sparsity under a newer wavelet transform. However, the reconstruction by our method is guided by structured sparsity theories to improve the reconstruction accuracy, no matter the type of wavelet transform. This is a main difference between our method and previous methods [41,42]. Our method can be applied for double-density dual-tree wavelet transform with small revisions on group setting.

## 5. Conclusion

We have proposed an efficient algorithm for CS-MRI. Our work has the following contributions. First, guided by structure sparsity theories, we introduce the tree sparsity to CS-MRI, and provide a convex formulation to model the tree structure combining with total variation and wavelet sparsity. It can substantially reduce the required undersampled data for CS-MRI. Second, an efficient algorithm with fast convergence performance is proposed in this paper to solve this model. Each iteration only costs $\mathcal{O}(NlogN)$ time for an image of size $N$. These properties make the practical CS-MRI much more feasible than before. Finally, our simulations and experiments on complexed-valued MR raw data demonstrate the superiority of the proposed algorithm to the state-of-the-art CS-MRI algorithms and several general tree-based algorithms or solvers in CS-MRI.

## Appendix A. The theoretical benefit of tree sparsity

Tree sparse data mean that the data are not only sparse or compressible, but also the support set yields a subtree structure. The tree sparse data have the tree sparsity property. In order to demonstrate the benefit of tree sparsity, we should first review the measurement bound for standard sparsity.

For inverse problem $Ax = b$, compressed sensing theory [7,8] guarantees the successful recovery of sparse data $x \in \mathbb{R}^N$ with only $M$ measurements ($M \ll N$). It assumes $A \in \mathbb{R}^{M \times N}$ is a randomly sampling matrix and satisfies the restricted isometry property (RIP) [44].

**Definition**. K-RIP

*For any matrix $A \in \mathbb{R}^{M \times N}$ and any integer $K < M$, for all $x$ in the union $\Omega_K$, if there exists a constant $\delta_K > 0$ and*

$$(1-\delta_K)\|x\|_2^2 \le \|Ax\|_2^2 \le (1+\delta_K)\|x\|_2^2$$

*the matrix A is said to satisfy the K-restricted isometry property with restricted isometry constant $\delta_K$.*

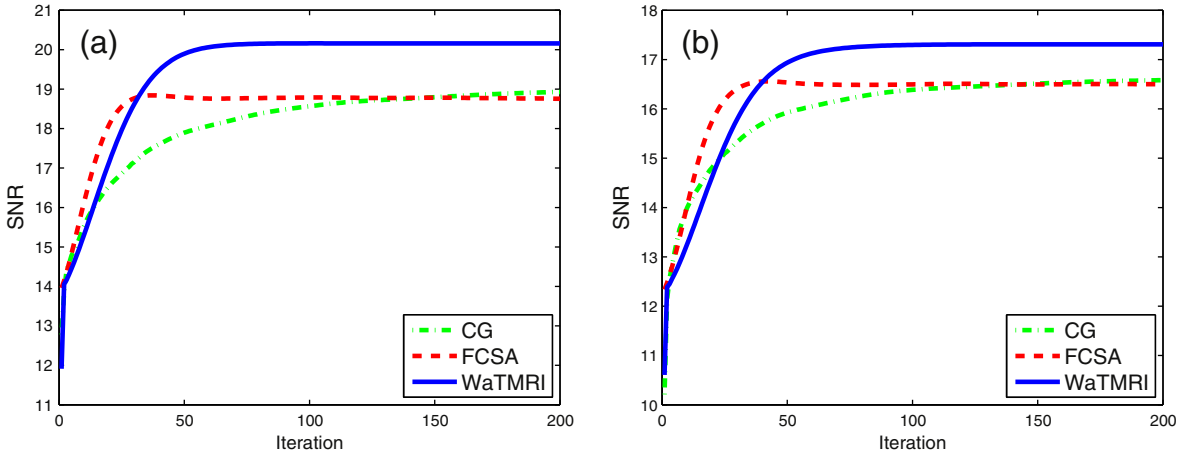


**Fig. 17.** Performance comparison on (a) 3 T brain image; (b) 1.5 T brain image.

$\Omega_K$ includes all the $C_N^K$ subspaces if there is no further constrain on the support set of sparse data $x$. However, when $x$ has some structured sparsity property(e.g. tree sparsity) and is in the union of subspaces $\mathcal{A}$, then the K-RIP can be extended to the $\mathcal{A}$-RIP [45]:

**Definition**. $\mathcal{A}$-RIP

*For any matrix $A \in \mathbb{R}^{M\times N}$, for all $x$ in the subspace $\mathcal{A}\in\mathbb{R}^N$, if there exist a constant $\delta_{\mathcal{A}}>0$ and*

$$(1-\delta_{\mathcal{A}})\|x\|_2^2 \le \|Ax\|_2^2 \le (1+\delta_{\mathcal{A}})\|x\|_2^2$$

*the matrix A is said to satisfy the $\mathcal{A}$-restricted isometry property with restricted isometry constant $\delta_{\mathcal{A}}$.*

For successful recovery, the number $M$ of required measurements has been quantified for a matrix $A$ has the $\mathcal{A}$-RIP [45]:

**Theorem 1**. $\mathcal{A}$-RIP

*Let $\mathcal{A}$ be the union of L subspaces of K dimension in $\mathbb{R}^N$. For any $t>0$,*

$$M \ge \frac{2}{c\delta_{\mathcal{A}_K}}\left(ln(2L)+KlnK\frac{12}{\delta_{\mathcal{A}_K}}+t\right) \tag{12}$$

*then there exists a randomly generated matrix $A\in\mathbb{R}^{M\times N}$ satisfy the $\mathcal{A}$-RIP with constant $c>0$ with probability at least $1-e^{-t}$.*

From (12), we could intuitively observe that $M$ can be less by reducing the number of subspaces $\mathcal{A}$. It coincides that the result will be improved when more priors are utilized. For standard $K$-sparse data, there is no more constrain to reduce the number of possible subspaces $C_N^K$. Therefore,

**Corollary.** *For K-sparse data, the sampling matrix A has the K-RIP with probability $1-e^{-t}$ if the bound for the number of measurements satisfies that $m=\mathcal{O}(K+Klog(N/K))$.*

For tree sparse data, the support of $x$ should follow the subtree structure. Then it is obviously that $\Omega_{Tree}\subset\Omega_K$ and $L_{Tree}<L_K$. And

**Lemma 1.** *For tree sparse data, the sampling matrix A has the $\mathcal{T}_K$-RIP with probability $1-e^{-t}$ if the bound for the number of measurements satisfies that:*

$$m=\mathcal{O}(K+log(N/K)) \tag{13}$$

**Proof.** The proof is conducted on the binary tree case for convenience. The bound for quadtree can be easily extended.

First, we need to figure out the number of subtrees (size $K$) of a binary tree (size $N$). Note that the root of the subtrees should be the binary tree's root.

**Case 1.** When $K\le\lfloor log_2N\rfloor$, the number of subtrees of size $K$ is just the Catalan number:

$$L_T=\frac{1}{K+1}\binom{2K}{K}\le\frac{(2e)^K}{K+1}\le\frac{e^KN}{K+1}$$

**Case 2.** When $K>\lfloor log_2N\rfloor$, the number of subtrees of size $K$ should follow [20]:

$$\begin{aligned}L_T &\le \frac{4^K}{K}\left(\frac{6}{\sqrt{\pi K}}ln\frac{log_2N}{log_2K)}+\frac{128}{e^2log_2K}\right)\\ &\le \frac{4^K}{K}\left(\frac{c_1log_2N}{log_2K)}+\frac{c2}{log_2K}\right)\\ &\le \frac{4^K}{K}\frac{c_1log_2(c_3N)}{log_2K}\\ &\le \frac{4^K(c_4N)}{K}\end{aligned}$$

where $c_1$, $c_2$, $c_3$, $c_4$ are some constants. Then we have:

$$L_T\le\begin{cases}\dfrac{e^KN}{K+1} & for\ K\le log_2N\\ \dfrac{4^K(c_4N)}{k} & for\ K>log_2N\end{cases} \tag{14}$$

According to Theorem 1:

$$M\ge\frac{2}{c\delta}\left(ln(2L_T)+Kln\frac{12}{\delta}+t\right) \tag{15}$$

With (16), the number of measurements should satisfy:

$$M\ge\begin{cases}\dfrac{2}{c\delta}(ln2+K+ln(N/(K+1))+Kln(12/\delta)+t)\\ \qquad for\ K\le log_2N\\ \dfrac{2}{c\delta}(ln2+Kln4+ln(c_4N/K)+Kln(12/\delta)+t)\\ \qquad for\ K>log_2N\end{cases} \tag{16}$$

for both cases, we have $M=\mathcal{O}(K+log(N/K))$ as the minimum number of measurements. Similar conclusion can be found in previous papers [20,21].

## References


[1] Pruessmann Klaas P, Weiger Markus, Scheidegger Markus B, Boesiger Peter. SENSE: sensitivity encoding for fast MRI. Magn Reson Med 1999;42(5):952–62.
[2] Griswold M, Jakob P, Nittka M, Goldfarb J, Haase A. Partially parallel imaging with localized sensitivities (PILS). Magn Reson Med 2000;44(4):602–9.
[3] Sodickson D, Manning W. Simultaneous acquisition of spatial harmonics (SMASH): fast imaging with radiofrequency coil arrays. Magn Reson Med 2005;38(4):591–603.
[4] Griswold M, Jakob P, Heidemann R, Nittka M, Jellus V, Wang J, et al. Generalized autocalibrating partially parallel acquisitions (GRAPPA). Magn Reson Med 2002; 47(6):1202–10.
[5] Lustig M, Pauly JM. SPIRiT: iterative self-consistent parallel imaging reconstruction from arbitrary k-space. Magn Reson Med 2010;64(2):457–71.
[6] Lustig M, Donoho D, Pauly J. Sparse MRI: the application of compressed sensing for rapid MR imaging. Magn Reson Med 2007;58(6):1182–95.
[7] Candès E, Romberg J, Tao T. Robust uncertainty principles: exact signal reconstruction from highly incomplete frequency information. IEEE Trans Inf Theory 2006;52(2):489–509.
[8] Donoho D. Compressed sensing. IEEE Trans Inf Theory 2006;52(4):1289–306.
[9] Liang D, Liu B, Wang J, Ying L. Accelerating SENSE using compressed sensing. Magn Reson Med 2009;62(6):1574–84.
[10] Beck A, Teboulle M. Fast gradient-based algorithms for constrained total variation image denoising and deblurring problems. IEEE Trans Image Process 2009;18(11):2419–34.
[11] Van Den Berg E, Friedlander M. Probing the pareto frontier for basis pursuit solutions. SIAM J Sci Comput 2008;31(2):890–912.
[12] Ma S, Yin W, Zhang Y, Chakraborty A. An efficient algorithm for compressed MR imaging using total variation and wavelets. Proc. IEEE Conf. Comput. Vis. Pattern Recognit. (CVPR); 2008. p. 1–8.
[13] Yang J, Zhang Y, Yin W. A fast alternating direction method for TVL1-L2 signal reconstruction from partial Fourier data. IEEE J Sel Top Signal Process 2010;4(2): 288–97.
[14] Huang J, Zhang S, Metaxas D. Efficient MR image reconstruction for compressed MR imaging. Proc. Medical image computing and computer-assisted intervention: Part I (MICCAI); 2010. p. 135–42.
[15] Huang J, Zhang S, Metaxas D. Efficient MR image reconstruction for compressed MR imaging. Med Image Anal 2011;15(5):670–9.
[16] Beck A, Teboulle M. A fast iterative shrinkage-thresholding algorithm for linear inverse problems. SIAM J Imaging Sci 2009;2(1):183–202.
[17] Manduca A, Said A. Wavelet compression of medical images with set partitioning in hierarchical trees. Proc. Int. Conf. IEEE Engineering in Medicine and Biology Soc. (EMBS), vol. 3; 1996. p. 1224–5.
[18] Said A, Pearlman W. A new, fast, and efficient image codec based on set partitioning in hierarchical trees. IEEE Trans Circ Syst Video Technol 1996;6(3): 243–50.
[19] Crouse M, Nowak R, Baraniuk R. Wavelet-based statistical signal processing using hidden markov models. IEEE Trans Signal Process 1998;46(4):886–902.
[20] Baraniuk R, Cevher V, Duarte M, Hegde C. Model-based compressive sensing. IEEE Trans Inf Theory 2010;56(4):1982–2001.
[21] Huang J, Zhang T, Metaxas D. Learning with structured sparsity. J Mach Learn Res 2011;12:3371–412.
[22] Bach F, Jenatton R, Mairal J, Obozinski G. Structured sparsity through convex optimization. Stat Sci 2012;27(4):450–68.

[23] Jenatton R, Mairal J, Obozinski G, Bach F. Proximal methods for hierarchical sparse coding. J Mach Learn Res 2011;12:2297–334.
[24] La C, Do M. Tree-based orthogonal matching pursuit algorithm for signal reconstruction. Proc. IEEE Int. Conf. Image Process. (ICIP); 2006. p. 1277–80.
[25] Rao N, Nowak R, Wright S, Kingsbury N. Convex approaches to model wavelet sparsity patterns. Proc. IEEE Int. Conf. Image Process. (ICIP); 2011. p. 1917–20.
[26] He L, Carin L. Exploiting structure in wavelet-based Bayesian compressive sensing. IEEE Trans Signal Process 2009;57(9):3488–97.
[27] He L, Chen H, Carin L. Tree-structured compressive sensing with variational Bayesian analysis. IEEE Signal Process Lett 2010;17(3):233–6.
[28] Som S, Schniter P. Compressive imaging using approximate message passing and a markov-tree prior. IEEE Trans Signal Process 2012;60(7):3439–48.
[29] Jacob L, Obozinski G, Vert J. Group lasso with overlap and graph lasso. Proc. 26th Annu. Int. Conf. Mach. Learn; 2009. p. 433–40.
[30] Chen C, Huang J. Compressive sensing MRI with wavelet tree sparsity. Proc. Adv. Neural Inf. Process. Syst. (NIPS); 2012. p. 1124–32.
[31] Ye J, Tak S, Han Y, Park H. Projection reconstruction MR imaging using FOCUSS. Magn Reson Med 2007;57(4):764–75.
[32] Chartrand R. Exact reconstruction of sparse signals via nonconvex minimization. IEEE Signal Process Lett 2007;14(10):707–10.
[33] Trzasko J, Manduca A. Highly undersampled magnetic resonance image reconstruction via homotopic $\ell$-0-minimization. IEEE Trans Med Imaging 2009;28(1):106–21.
[34] Baraniuk R, DeVore R, Kyriazis G, Yu X. Near best tree approximation. Adv Comput Math 2002;16(4):357–73.
[35] Tropp J, Gilbert A. Signal recovery from random measurements via orthogonal matching pursuit. IEEE Trans Inf Theory 2007;53(12):4655–66.
[36] Wright S, Nowak R, Figueiredo M. Sparse reconstruction by separable approximation. IEEE Trans Signal Process 2009;57(7):2479–93.
[37] Liu S, Ji J. Ye, Slep: Sparse learning with efficient projections. Arizona State University; 2009.
[38] Deng W, Yin W, Zhang Y. Group sparse optimization by alternating direction method, TR11–06. Department of Computational and Applied Mathematics, Rice University; 2011.
[39] Nesterov Y. A method of solving a convex programming problem with convergence rate o(1/k2). Soviet Math. Dokl., vol. 27; 1983. p. 372–6.
[40] Nesterov Y. Gradient methods for minimizing composite functions, preprint 2013;140(1):125–61.
[41] Kim Y, Altbach M, Trouard T, Bilgin A. Compressed sensing using dual-tree complex wavelet transform. Proc. Intl. Soc. Mag. Reson. Med, vol. 17; 2009. p. 2814.
[42] Zhu Z, Wahid K, Babyn P, Yang R. Compressed sensing-based mri reconstruction using complex double-density dual-tree DWT. Int J Biomed Imaging January 2013;2013(10).
[43] Selesnick IW. The double-density dual-tree DWT. IEEE Trans Signal Process 2004;52(5):1304–14.
[44] Candes E, Tao T. Decoding by linear programming. IEEE Trans Inf Theory 2005;51(12):4203–15.
[45] Blumensath T, Davies M. Sampling theorems for signals from the union of finite-dimensional linear subspaces. IEEE Trans Inf Theory 2009;55(4):1872–82.